

This Page Is Inserted by IFW Operations  
and is not a part of the Official Record

## **BEST AVAILABLE IMAGES**

Defective images within this document are accurate representations of the original documents submitted by the applicant.

Defects in the images may include (but are not limited to):

- BLACK BORDERS
- TEXT CUT OFF AT TOP, BOTTOM OR SIDES
- FADED TEXT
- ILLEGIBLE TEXT
- SKEWED/SLANTED IMAGES
- COLORED PHOTOS
- BLACK OR VERY BLACK AND WHITE DARK PHOTOS
- GRAY SCALE DOCUMENTS

**IMAGES ARE BEST AVAILABLE COPY.**

**As rescanning documents *will not* correct images,  
please do not report the images to the  
Problem Image Mailbox.**

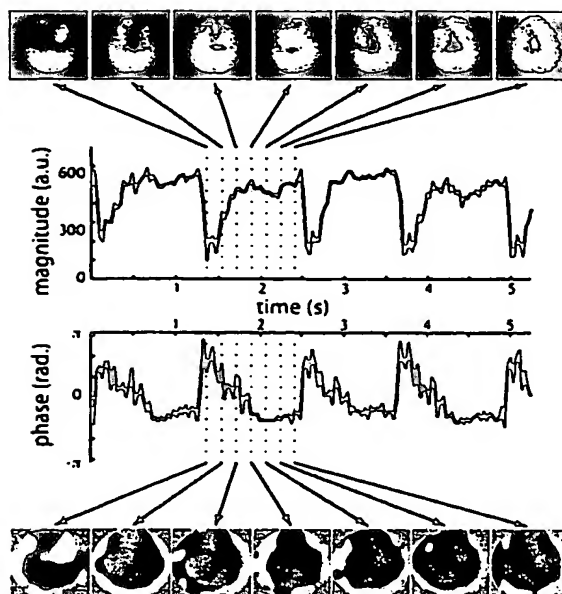


FIG. 1. Illustration of the effects of motion on DW magnetization. The magnitude (top) and phase (bottom) of a series of low-resolution axial single-shot DWI images (2D navigators) are shown over a single cardiac cycle. The magnitude and phase of a representative voxel are plotted in the middle over four cardiac cycles. The spatial variation in the image magnitude and phase is nonlinear and strongly correlated to the cardiac cycle.

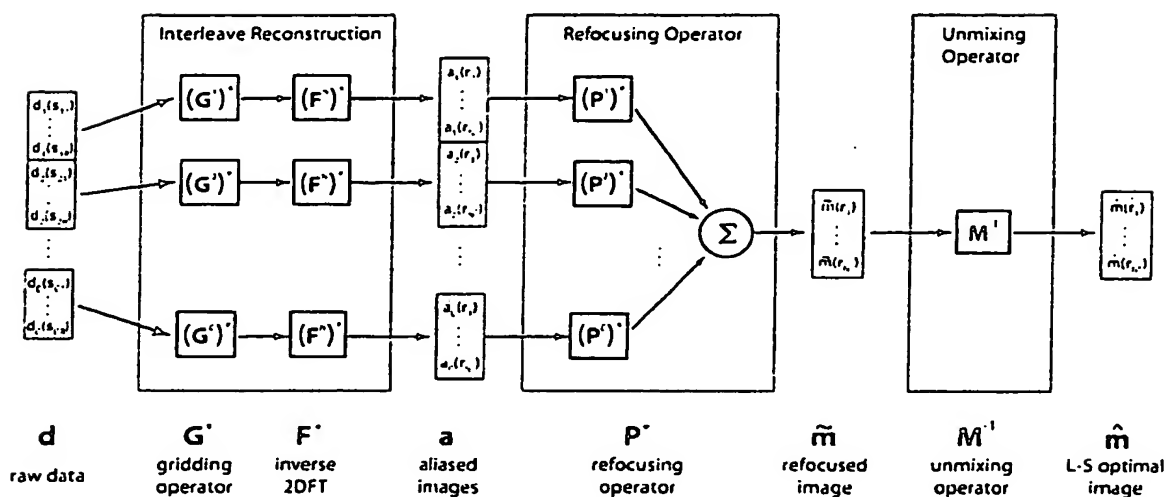


FIG. 2. Diagram of the least-squares matrix reconstruction given in Eq. [2]. Each raw data interleave  $d_i$  is gridded and inverse Fourier-transformed by the interleave reconstruction to form an aliased image  $a_i$ . These images are phase-corrected and summed by the refocusing operator to form the refocused image  $\tilde{m}$ . Remaining aliased energy is removed by the unmixing operator  $M^{-1}$  to give the least-squares optimal image  $\hat{m}$ . If the aliased energy in the refocused image is sufficiently low, the reconstruction can stop at  $\tilde{m}$ , avoiding the computationally expensive inverse calculation  $M^{-1}$ . In this case, we call the algorithm a "refocusing reconstruction."

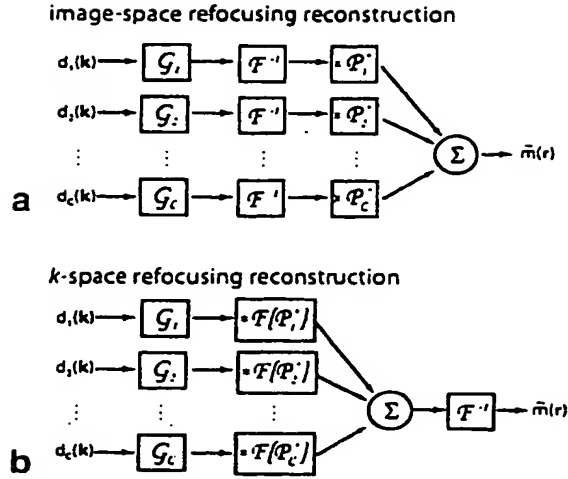


FIG. 3. Block diagram of two versions of the refocusing reconstruction in which refocusing is performed in (a) image space and (b)  $k$ -space. The boxed expressions indicate the operations of gridding ( $G_j$  grids the  $j$ th readout trajectory), inverse Fourier transform ( $F^{-1}$ ), and refocusing (multiplication by  $P_j^*(r) = e^{-i\phi_j(r)}$  in image-space or convolution by  $F[P_j^*]$  in  $k$ -space).

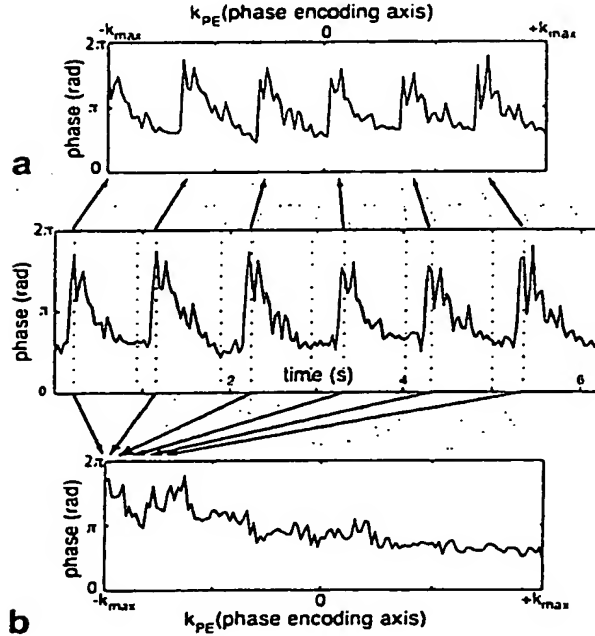


FIG. 4. The effect of 2DFT phase-encode ordering on  $k$ -space. The phase history of a representative voxel over time is shown in the middle plot. The gray swathes represent cardiac-gated imaging windows. The  $k$ -space modulation imparted by this phase history is shown for (a) standard incremental phase-encode ordering and (b) an alternate phase-encode ordering. The latter ordering interleaves the data from different cardiac cycles to achieve a smoother modulation.

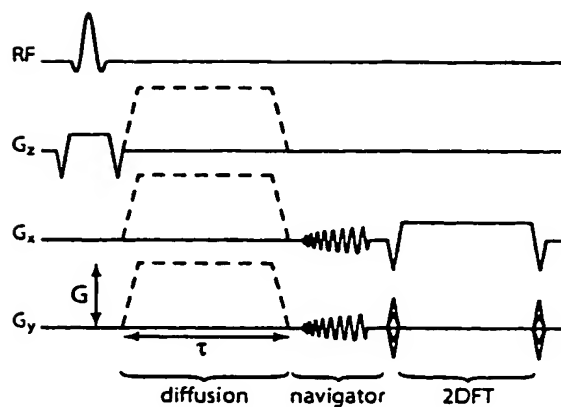


FIG. 5. Navigated steady-state DWI pulse sequence used in this study. The sequence is fully refocused except for the diffusion gradient (with amplitude  $G$  and duration  $\tau$ ), which rephases DW echoes over multiple TRs.

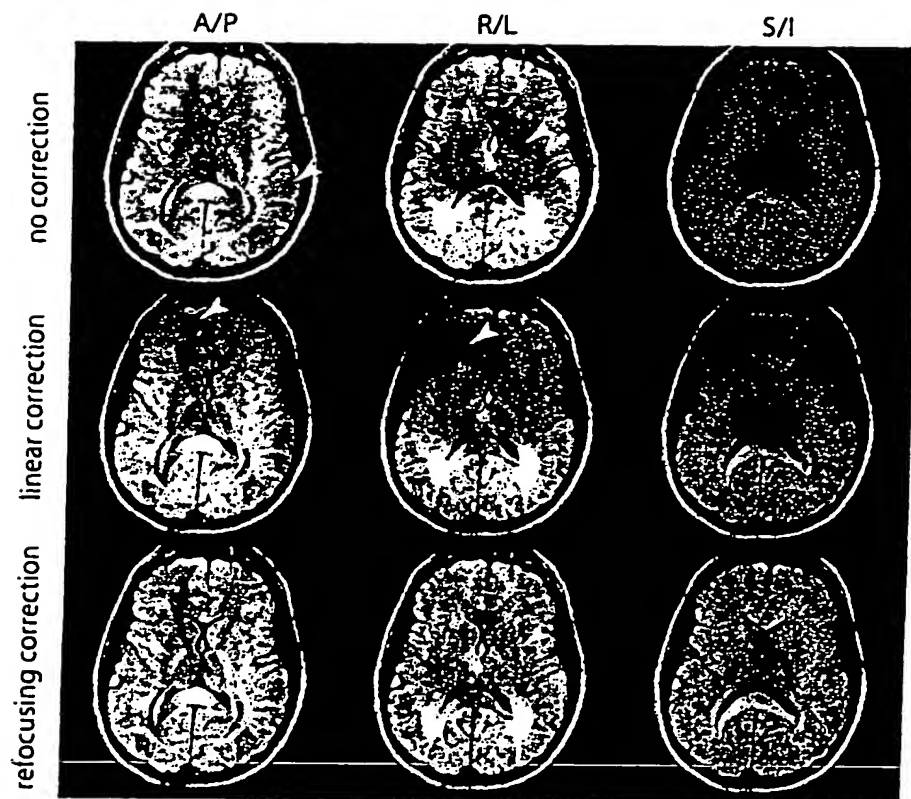


FIG. 6. Untriggered spiral-navigated 2DFT images with varying levels of correction. Rows (from top to bottom) have no correction, the standard linear correction, and the refocusing correction. Columns (from left to right) show images with diffusion weighting along the A/P, R/L, and S/I directions. Arrows in the A/P- and R/L-weighted uncorrected images (top row) indicate examples of dephasing due to motion. Arrows in the middle row indicate artifacts introduced by the linear correction. Arrows in the bottom row indicate structures with increased conspicuity after the refocusing correction.

# BEST AVAILABLE COPY

FIG. 7. Cardiac-synchronized, spiral-navigated 2DFT images acquired with the phase-encode interleaving scheme shown in Fig. 4. Diffusion weighting is along the (a) A/P, (b) R/L, and (c) S/I directions.

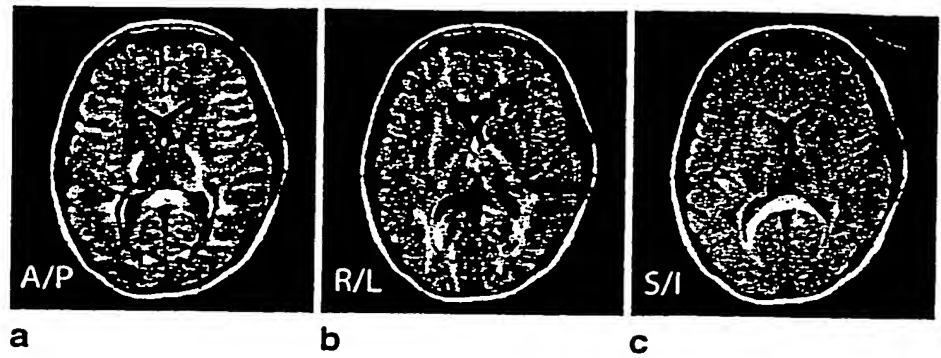
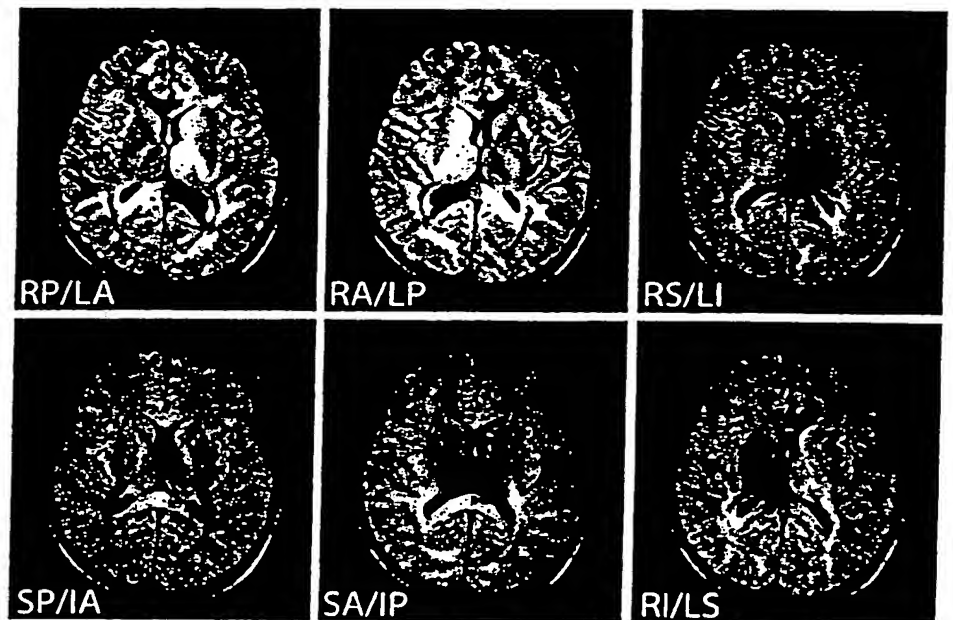


FIG. 8. Navigated SS-DWI images acquired with diffusion weighting along the standard directions for diffusion tensor. Images are cardiac-synchronized and were reconstructed using the refocusing reconstruction.



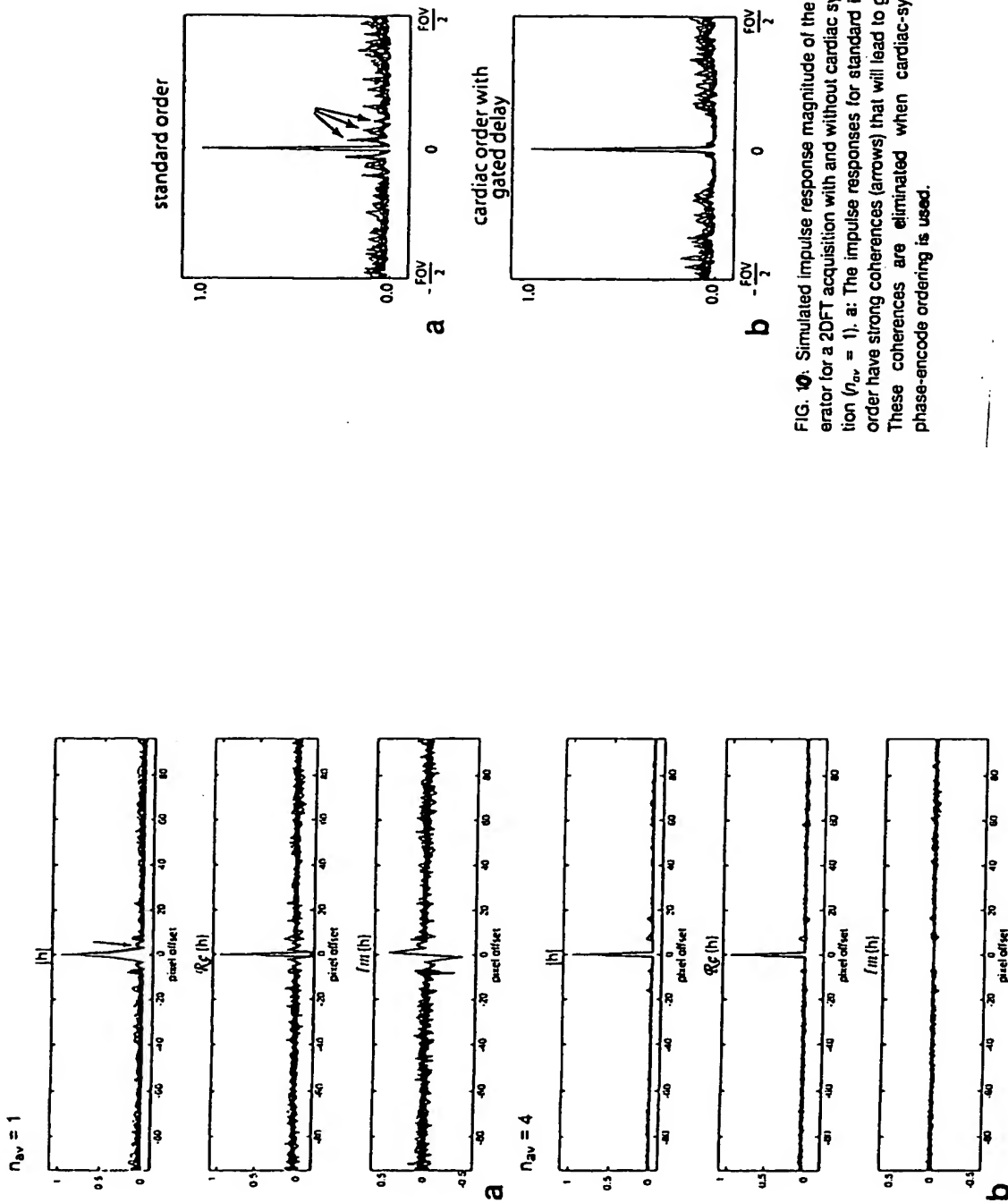


FIG. 9. Impulse responses of the mixing operator for a 2DFT acquisition with (a) no averaging and (b) four averages. Each subfigure overlays the impulse responses for the same 10 voxels taken from a representative navigator data set. The arrow in a indicates coherences in the mixing impulse responses that lead to coherent ghosts. Averaging in b suppresses much of the off-peak energy.

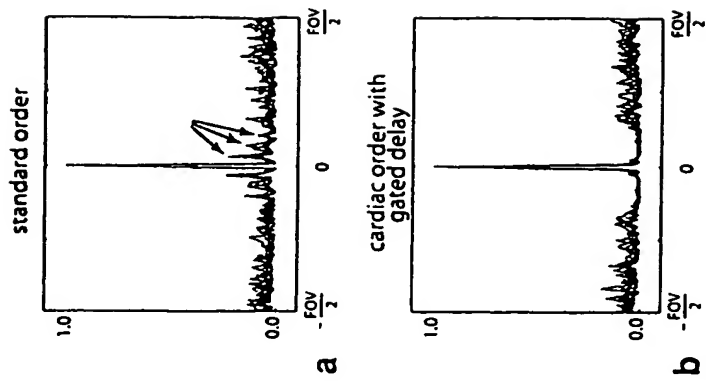


FIG. 10. Simulated impulse response magnitude of the mixing operator for a 2DFT acquisition with and without cardiac synchronization ( $n_{av} = 1$ ). a: The impulse responses for standard incremental order have strong coherences (arrows) that will lead to ghosting. b: These coherences are eliminated when cardiac-synchronized phase-encode ordering is used.